frontiers | Frontiers in Materials

TYPE Original Research
PUBLISHED 17 October 2024
DOI 10.3389/fmats.2024.1470651

OPEN ACCESS

EDITED BY
Xuewei Fang,
Xi'an Jiaotong University, China

REVIEWED BY
Changjun Han,
South China University of Technology, China
Lakshmi Narayan Ramasubramanian,
Indian Institute of Technology Delhi, India

*CORRESPONDENCE
Rustam R. Kyarimov,
rustam.kyarimov@skoltech.ru

RECEIVED 25 July 2024
ACCEPTED 03 October 2024
PUBLISHED 17 October 2024

CITATION
Kyarimov RR, Statnik ES, Sadykova IA, Frantsuzov AA, Salimon AI and Korsunsky AM (2024) Factorial-experimental investigation of LPBF regimes for VZh159 nickel superalloy grain structure and structural strength optimization.
Front. Mater. 11:1470651.
doi: 10.3389/fmats.2024.1470651

Factorial-experimental investigation of LPBF regimes for VZh159 nickel superalloy grain structure and structural strength optimization

Rustam R. Kyarimov[1]*, Eugene S. Statnik[1,2], Iuliia A. Sadykova[1], Alexander A. Frantsuzov[1], Alexey I. Salimon[1,2] and Alexander M. Korsunsky[1,2,3]

[1]HSM Lab, Center for Digital Engineering, Skoltech, Moscow, Russia, [2]CASM&T, Moscow Aviation Institute, Moscow, Russia, [3]Professor and Fellow Emeritus, Trinity College, Oxford, United Kingdom

This study investigates the optimization of Laser Powder Bed Fusion (LPBF) process parameters to enhance the mechanical properties of the Russian Ni superalloy VZh159 (a close analogue of IN718) material that is commonly used in critical aerospace applications, and the corresponding studies of the grain structure within and near the melt pool formed by a single laser scan line. Through a factorial experimental approach, the influence of laser power and scanning speed on the tensile strength, yield strength, and ductility was determined. Metallurgically sound samples (based on hydrostatic weighing data and microscopy, with practically no pores detected) were obtained with nine combinations of power and scanning speed, showing significant variation in the tensile strength (in the 1,040–1,220 MPa range) and yield strength (in the 560–1,100 MPa range), which correlated with the cross-sectional area of the single scan line (for example, the depth of the melt pool varied in the range 410–530 μm), while the average grain size (deduced from Electron Backscatter Diffraction (EBSD) images) remained statistically unchanged. Key findings indicate that the optimal LPBF parameters are a laser power of 250 W, a scanning speed of 600 mm/s, and a hatch distance of 0.12 mm, which together yield the best combination of high tensile strength and ductility. This study provides new insights into the effects of LPBF parameters on the microstructure, particularly the formation of the γ′ strengthening phase and its correlation with mechanical performance. The research addresses a critical gap in understanding the relationship between LPBF processing conditions and the resulting microstructural and mechanical properties, offering potential improvements in manufacturing efficiency and material performance.

KEYWORDS

additive manufacturing, laser powder bed fusion, melt pool, electron microscopy, experimental design, rational experimental-computational correlation

1 Introduction

It is often intuitively believed that additive manufacturing technologies (that are, in fact, rooted in prehistoric practices such as pottery) have advantages over subtractive counterparts in terms of reducing raw material costs and possibly tooling costs. This aligns with the sharply increased public expectations regarding "green" technologies in the 2000s. The digitization of industrial production, which has been a persistent trend for the last 50 years, combined with additive manufacturing, has ultimately given rise to a range of technologies, notably LPBF, that combines relatively tight dimensional tolerances, high shape complexity, and high productivity. This advantageous combination has attracted attention even in the industries with the highest demands for material integrity, and hence for the absence of defects, dimensional tolerances, surface smoothness, reproducibility of structure, and other properties. Almost nowhere are these requirements as stringent as in the civil aerospace and rocket engine manufacturing (Prashar et al., 2022).

High performance titanium alloys for the compressor section, and heat-resistant metallic materials such as steels, and nickel superalloys for the combustion chamber and the turbine used in modern jet engines are at the focus of worldwide research in the context of LPBF manufacturing, with a significant number of publications produced annually (Adegoke et al., 2020; Bernard et al., 2023; Khanna et al., 2021). This research covers various aspects of LPBF, including the precise formulation of alloys (Aota et al., 2020), powder production (manufacturing, storage, and preparation) (Badoniya et al., 2024; Gokcekaya et al., 2021; Ruan et al., 2022), 3D printing equipment and printing strategies (substrates, fill factor, fill pattern) (LPBF, 2024; Pelevin et al., 2023; Pant et al., 2022), printing parameters (power, scanning speed, focus size, and overlap) (Evangelou et al., 2023; Paraschiv et al., 2022; Qin et al., 2023), post-processing and machining (heat treatment, hot isostatic pressing, plastic deformation) (Bologna et al., 2024; Ge et al., 2023; Diniță et al., 2023), quality and dimensional stability (Pant et al., 2023; Cao et al., 2021) and control and management of the structure (Livera et al., 2024; Huang et al., 2024; Hasanabadi et al., 2023), as well as testing and certification (Taylor et al., 2021; Gibbons et al., 2021; department of transportation, 2024). Computer modeling is rapidly advancing to provide theoretical support for empirical research (Dimopoulos et al., 2023; Khorasani et al., 2020). However, it is believed that carefully planned experiments must play a crucial role to validate these computational predictions through the use of rational experimental–computational correlation (RECC).

Nickel superalloys for turbine blades in jet engines are of particular interest for LPBF manufacturing and repair (Shrivastava et al., 2021), as this technology addresses several issues associated with traditional casting and mechanical processing of forged billets, such as incorporation of intricate internal channels and cavities, precise geometry, and the ability to repair or refurbish damaged or worn components. IN718 is one of the most extensively studied nickel superalloys, and many recent publications address the fundamental issues of applying LPBF to IN718 (Yong et al., 2020; Rafael De Sa Barros, 2019; Salvati et al., 2020). VZh159 (Kablov et al., 2020) is the Russian equivalent of IN718. This report is devoted to a series of experiments, varying laser power and scanning speed to control the mechanical properties (yield strength, tensile strength, elongation to failure) and grain structure characteristics. Single laser scan line tests were conducted by LPBF deposition of material on the top surfaces of a forged nickel alloy plate to reveal the grain structure formation in the melt pool and to correlate it with the mechanical properties. Thus, the general materials science approach is applied that consists of establishing the correlation between structure and properties for the specific case of LPBF nickel superalloy VZh159 as an example.

While extensive studies have been conducted on IN718, a widely used nickel superalloy, less attention has been given to its Russian equivalent, VZh159, despite its potential in similar high-temperature applications. This study aims to fill this gap by investigating the LPBF process parameters that affect the mechanical properties of VZh159, thereby contributing to the broader understanding of Ni-based superalloys in additive manufacturing.

The novelty of this research lies in its use of a full factorial experimental design to systematically explore the effects of laser power and scanning speed on mechanical properties, such as tensile strength, yield strength, and ductility. Additionally, consideration is given to how these parameters influence the formation of the γ' strengthening phase and its distribution within the microstructure, offering new insights into the correlation between LPBF process conditions and alloy performance was examined.

2 Materials and methods

2.1 Sample preparation

In the study, samples were produced from the metal powder (particle size of 15–45 μm) of the heat-resistant alloy VZh159 (Amet, Asha, Russia) by the LPBF method using the SLM 280 HL machine (SLM Solutions GmbH, Lübeck, Germany). The chemical composition of VZh159 shown in Table 1 is close to that of IN718.

In order to determine the optimal printing parameters for the system, 27 flat plates with the dimensions of 2 × 15 × 70 mm (thickness, width, length) were produced under nine different regimes (three samples per each regime), with the laser power and scanning speed varied within the ranges of 250, 300, 350 W and 600, 700, 800 mm/s, respectively. The hatch distance across the entire range of conditions remained unchanged at 0.12 mm. The scanning rotation angle was 67°. The powder layer thickness was 50 μm. The designation of sample hereinafter has the format VZh159-Power-Scanning Speed, e.g., VZh159-250-700. The plates were manufactured along the direction of the recoater's movement. The fabrication of plates in the recoater movement direction is justified to minimize the risk of damaging adjacent samples under building if one of them detaches, in case the melting regimes turn out to be unsuitable for forming a suitable structure from the VZh159 metal powder.

The experiments involving the deposition of nine single scan lines on the flat plates with the dimensions of 20 × 20 × 5 mm (width, length, thickness) made from VZh159 alloy that was manufactured by LPBF and, separately, as-forged, - were conducted using a similar combination of melting parameters (laser power and scanning speed) as used in the production of sample plates by LPBF.

TABLE 1 Chemical composition of the chromium-nickel alloys VZh159 and IN718 (in wt%).

	Ni	Cr	Al	Mo	Si	Mn	Fe	P	S	C	Nb	N	O
VZh159	59.68	26.7	1.52	7.2	0.75	0.22	0.76	0.004	0.004	0.056	2.9	0.19	0.013
IN718	52.5	19	0.5	3.05	0.35	0.35	16.8	0.015	0.015	0.08	5.13	-	-

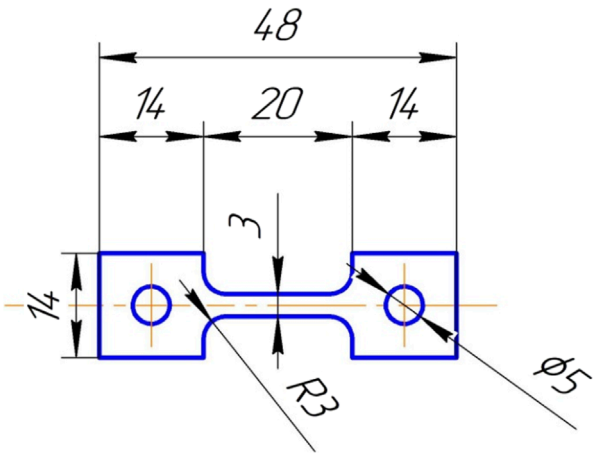

FIGURE 1
Geometrical dimensions of the sample cut from plates manufactured using LPBF.

2.2 Tensile testing

The mechanical tests were conducted using a universal testing machine IR 5113-100-11 (Tochpribor, Ivanovo, Russia) in accordance with GOST 11701-84 standard. Prior to the test, samples with the dimensions of 2 × 3 × 48 mm (thickness, width of the test section, length) were cut from the printed plates and subjected to a slight polishing process (Figure 1). Subsequently, the samples were tested in tension until failure. The stress-strain curves for the 27 samples are shown in Figure 5.

2.3 Microstructure characterization

To investigate the microstructure with the corresponding melt pool of a single scan line, the cross-section of the plate was deliberately ground and polished according to the following steps. The initial step involved cutting the plate with 9 laser scan lines to the required dimensions using Accutom-100 cutting machine (Struers, Denmark). The cutting parameters included the speed of 3000 RPM and the feed rate of 0.3 mm/s with a diamond-tipped cutting disc of B0D15 grade. After the cutting process, the plate was progressively ground using silicon carbide sandpaper with grit sizes of 220, 320, 500, 800, 1,000, and 2000 to achieve smooth surface finish. The plate then underwent intermediate polishing using coarse polishing cloths with diamond suspensions of 6, 3, and 1 μm grain sizes, along with MD-Lubricant Green from MD-Chem for the 6 and 3 μm suspensions, and MD-Mol for the 1 μm suspension. For the final polishing process, fine MD-Chem cloths were used together with Oxide Polishing Suspensions (OPS), to achieve a mirror-like finish. Grinding and polishing were carried out using LaboSystem equipment and consumables from Struers. The final stage of plate preparation involved ion etching, which was performed to remove any amorphous surface layers and enhance the microstructural features of the surface. This process was performed using a Leica ion etcher (Leica Microsystems, Germany) under high vacuum conditions. The parameters used were the ion beam energy of 5 keV, etching angle of 3°, and etching time of 15 min.

EBSD mapping was performed using JEOL JSM-IT500 scanning electron microscope with Bruker eFlash FS detector. The plate was tilted by 70° to the electron beam and the tilt correction was performed using a built-in function of the microscope software to obtain undistorted surface images. Accelerating voltage was set at 20 kV, working distance – 19 mm and the distance between the sample and the detector was 16 mm according to generally accepted recommendations. Exposure time was set to 10 ms, as it provided high quality results with low amount of zero solutions and the binning of 2 × 2 was applied. Acquired map size was ~890 × 670 μm, which allowed capturing the full depth of the melt pool for all regimes.

The determination of porosity in the manufactured samples of VZh159 alloy was carried out in accordance with GOST R 57,910-2017″Materials for additive technological processes. Control and test methods of metal raw materials and products” (Materials for additive technological processes, 2024), while the determination of density was performed in accordance with GOST 20018-74 (CT CMEA 1253-78, ISO 3369-75) “Sintered hardmetals. Determination of density”.

3 Results

3.1 Parameter optimization

To determine the optimal melting parameters, a full factorial experimental Table 3×3^2 was used (two factors varied at three levels). Two parameters were changed during the experiment: scanning speed (v) and laser power (P) at three levels, while layer thickness (t) and laser hatching distance (h) were kept fixed. These technological parameters are the key factors affecting the manufacturing quality. The laser power (parameter X_1) and the scanning speed (parameter X_2) were chosen as the varying factors. Tensile strength (σ_T) (variable Y) was chosen as the dependent variable (Novik and Arsov, 1980; Kyarimov et al., 2023; Lankin and Shaikhutdinov, 2015). For the dependent variable Y the tensile strength of the samples σ_T, at a 95% confidence level, the coefficients b_{112}, b_{122}, b_{1122}, were found to be statistically insignificant and were

10.3389/fmats.2024.1470651

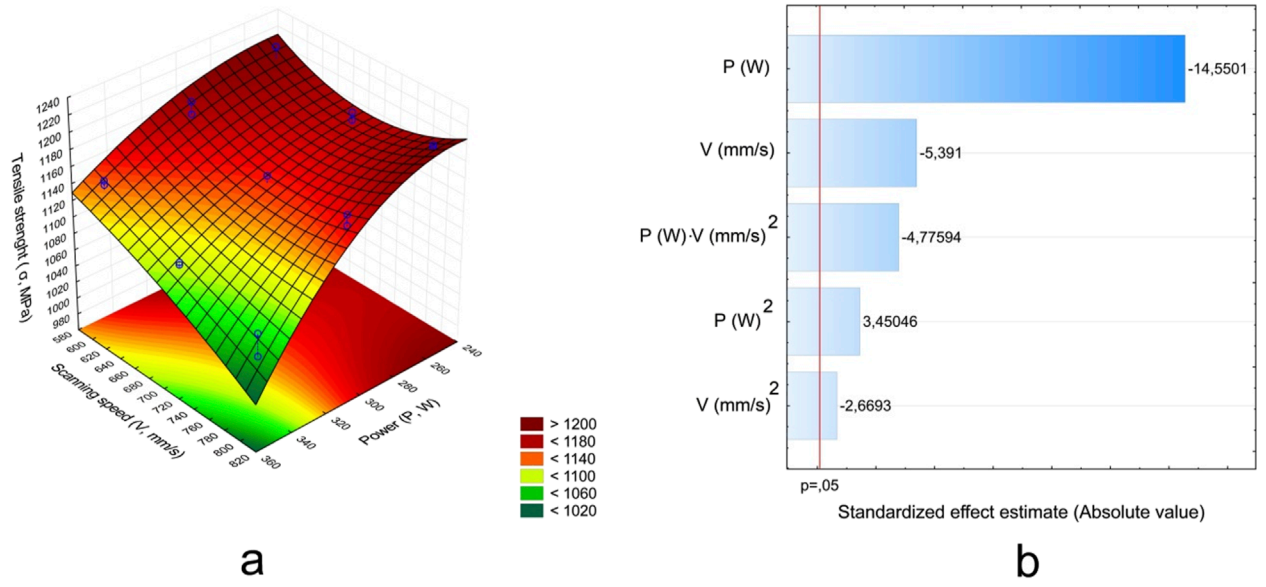

FIGURE 2
(A) Dependence of the tensile strength on the technological parameters of melting. **(B)** Pareto chart for tensile strength.

excluded from the regression model. The values of the statistically significant regression coefficients are as follows:

$$b_0 = 1148.27, b_1 = -46.12, b_2 = -17.09, b_{11} = 9.47, b_{22} = -7.33, b_{12} = -18.54$$

The regression equation for the unencoded factor levels is as follows:

$$\sigma_T = 1148.27 - 46.12 \cdot P - 17.09 \cdot V + 9.47 \cdot P^2 - 7.33 \cdot V^2 - 18.54 \cdot P \cdot V \quad (1)$$

Figure 2A shows the graphical representation of the regression model (Equation 1), depicting the relationship between the variable Y and the influence of technological parameters, laser power and the scanning speed. The greatest influence on the tensile strength of the samples, within the intervals of variation chosen for this study, is exerted by the laser power. Figure 2B presents the Pareto chart of significant effects for the dependent variable of tensile strength. Among the chosen intervals, the quadratic scanning speed had the least impact on the tensile strength. The maximum tensile strength is achieved with the following combination of scanning technological parameters: laser power of 250 W and scanning speed of 600 mm/s.

To determine the influence of 9 melting regimes on the yield strength (σ_y), statistical analysis of the obtained data was conducted. The dependent variable chosen was Y the yield strength (σ_y). Laser power P (parameter X_1) and scanning speed v (parameter X_2) were selected as the varying parameters. For the dependent variable Y the σy, at a 95% confidence level, the coefficients b_{22} and b_{1122} were found to be statistically insignificant and were excluded from the regression model. The developed regression model accounted for second-order interactions of factors. The values of the statistically significant regression coefficients are as follows:

$$b_0 = 721.8, b_1 = -152.26, b_{11} = -56.35, b_2 = -79.97, b_{12} = 91.25,$$
$$b_{112} = 48.75, b_{122} = -33.32$$

The regression equation for the influence of melting technological parameters on yield strength, for unencoded factor levels, is as follows:

$$\sigma_Y = 721.8 - 152.26 \cdot P - 56.35 \cdot P^2 - 79.97 \cdot V + 93.25 \cdot P \cdot V + 48.75 \cdot P^2 \cdot V - 33.32 \cdot P \cdot V^2 \quad (2)$$

Figure 3A presents the graphical representation of the regression model (Equation 2), showing the dependence of the variable Y on the influence of technological parameters, the laser power and the scanning speed. The maximum yield strength is achieved with the following combination of melting technological parameters: laser power of 250 W and scanning speed of 600 mm/s. Figure 3B presents the Pareto chart of significant effects for the dependent parameter of yield strength. Among the factors studied, laser power has the greatest influence on the yield strength of the samples within the chosen intervals. The least impact on yield strength was caused by the product of laser power and the square of the scanning speed.

Each factor had three levels, and the experiment was conducted with all possible combinations of these levels. Quadratic interdependencies between parameters and variables refer to models that include nonlinear (quadratic) effects of the factors (such as P^2, V^2, P × V). The dependencies of the variables (factors: laser power "P" and scanning speed "V") were considered beyond the first order, meaning that the response change was not a linear function of the factors, but also included quadratic terms. This approach made it possible to account for more complex relationships between the factors and the response that cannot be captured using a linear model. The regression equation with second-order variables allowed

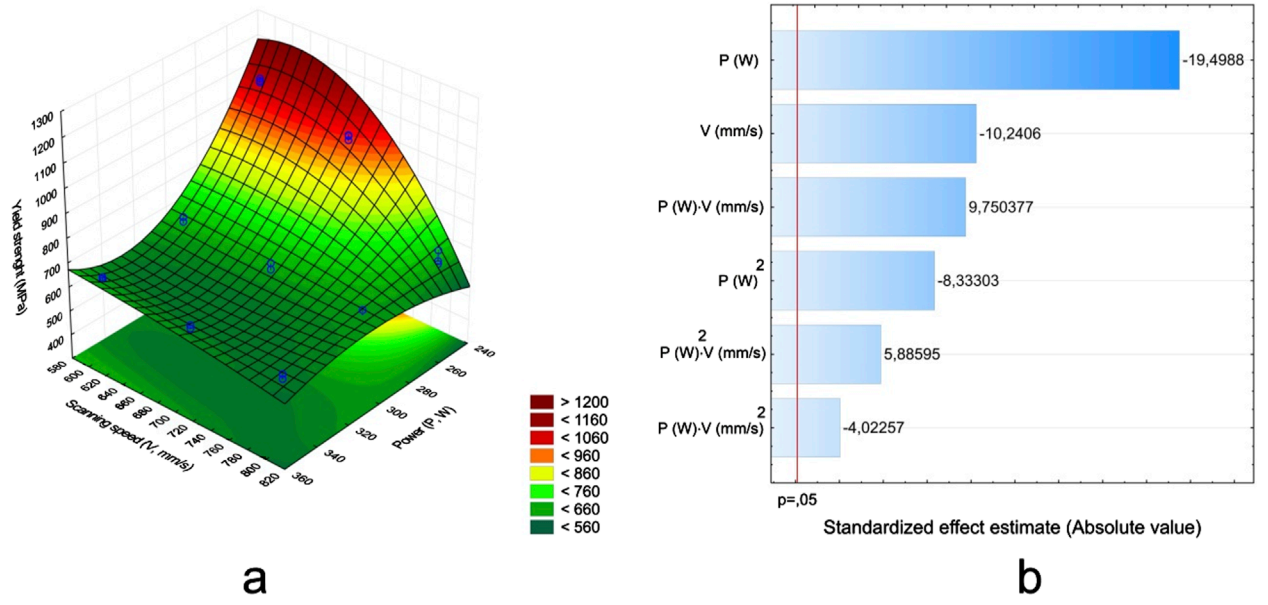

FIGURE 3
(A) Dependence of the yield strength on the technological parameters of melting. **(B)** Pareto chart for yield strength.

for a more comprehensive assessment of the influence of the factors (P, V) on the response, providing a deeper understanding of how these parameters affect the mechanical properties.

To compare VZh159 with other analogs and their properties, a review of similar alloys by chemical composition was conducted using the Granta Ansys Selector 2021 software with SENVOL database (Senvol Database, 2024). Data from 9 different LPBF regimes were added to the Ashby chart, relating the ultimate tensile strength to the yield strength, for comparing the obtained values for VZh159 with similar Ni-based alloys (Figure 4). The most of LPBF regimes (7 of 9) return noticeably lower yield strength and higher ultimate tensile strength than standard forged and solution treated IN718. On the other hand, the same LPBF regimes show mechanical performace fairly comparable with the same characteristics reported for IN718 3D-printed at widely used EOS, SLM Solution and Trumpf machines. In general, 3D-printed IN718 before post-processing (single or multi-stage aging) is similar to the solution-treated traditional forged IN718 (although somewhat lower yield strength and higher ultimate tensile strength may be observed).

Surprisingly, the two LPBF regimes (VZh159-250-600 and VZh159-250–700) applied to VZh159 bring this alloy to the mechanical performance similar to solution-treated and aged IN718. This effect is believed to be directly related with the peculiarities of thermal history during manufacturing. This interrelation must be carefully analyzed and discussed considering the following aspects:

- Overall metallurgical quality – homogeneity and porosity;
- Grain structure (grain size and shape aspects) and texture;
- Phase state – the presence of the reinforcing γ-phase;
- Residual stress at inter- and intragranular level.

One can notice that optimal regimes (250–600 and 250–700) showcase both high yield strength and further near pure plasticity with almost no work-hardening. Other regimes tend to shift mechanical performance towards another character of stress-strain curves - low yield strength and strong work-hardening. Few regimes (300–700 and 300–800) may bring both types of stress-strain curves suggesting the unevenness of microstructure (Figure 5).

The hydrostatic density test data, as well as the elongation at break–some of the potential indices sensitive to metallurgical quality, such as homogeneity and residual porosity in LPBF–are presented in Table 2.

The actually measured density of samples manufactured from VZh159 differs from the theoretical density by approximately 3.6%, which may indicate slight porosity. However, it should be noted that the theoretical density of the VZh159 metal powder is approximately 8.1–8.3 g/cm^3, and this value may vary depending on the manufacturer and the characteristics of the specific powder batch. Considering the density obtained within the selected range of melting regimes, it averages 7.88 g/cm^3. The densities across all conditions vary only slightly, indicating satisfactory metallurgical strength of the 3D-printed VZh159 and potentially reflecting the stability of the melting process.

3.2 Single laser scan line microstructure study

After determining the optimal regimes for laser powder bed fusion of VZh159 metal powder through the correlation of data obtained from both computational and experimental methods, the melt pools were studied for 9 LPBF regimes. The melt pools were formed by depositing single laser scan line with the thickness of one pass of laser hatch distance on a metal plate, and subsequently determining the depth and width in the cross-section (Figure 6). The

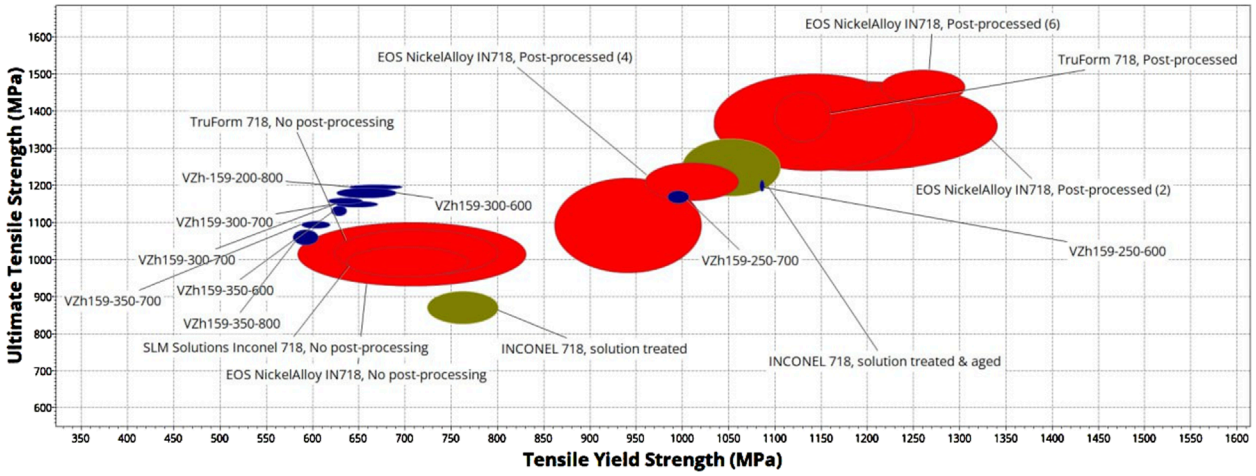

FIGURE 4
The relationship between ultimate tensile strength to yield strength for Ni based alloys and VZh159.

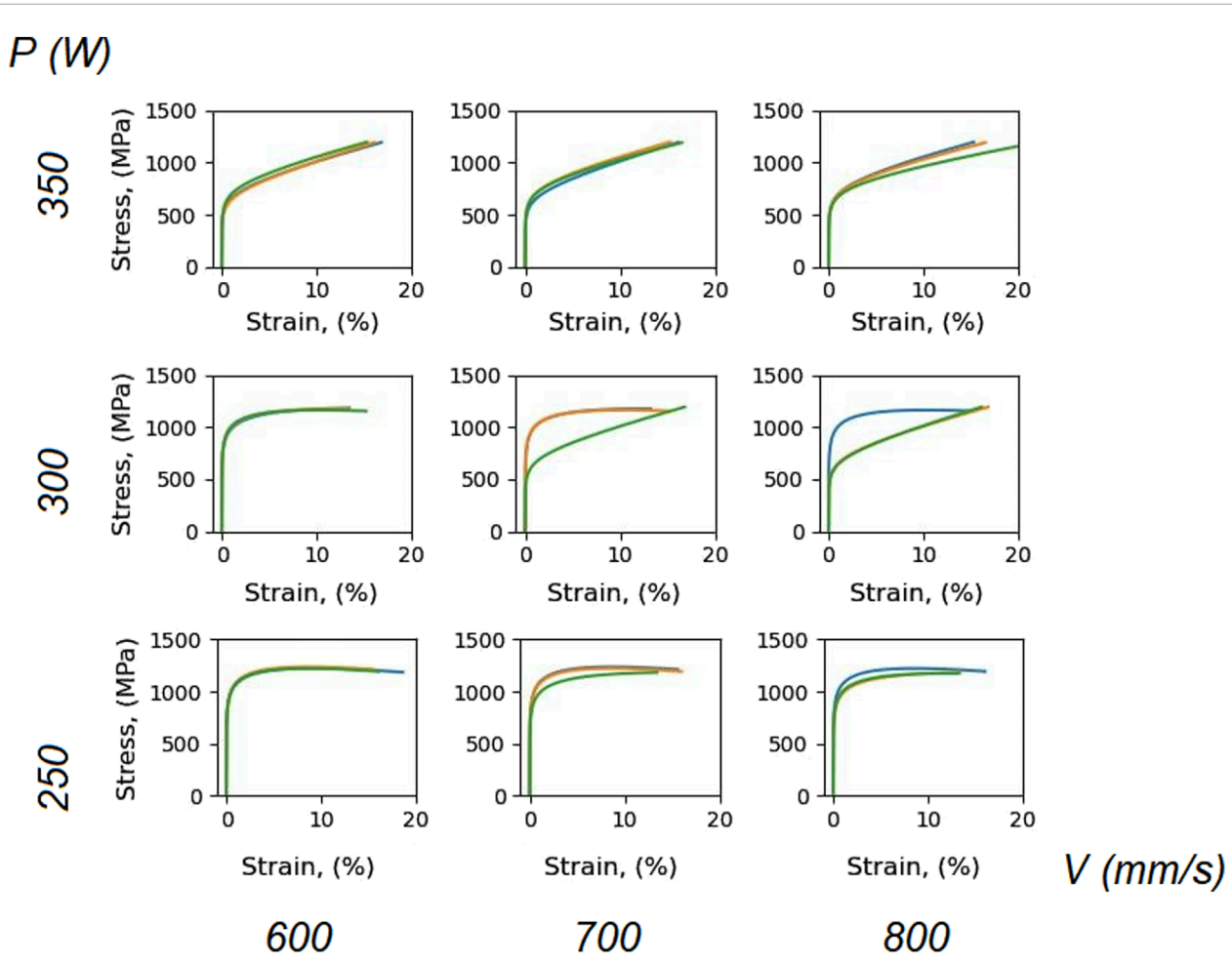

FIGURE 5
Stress-strain curves for the 27 samples.

10.3389/fmats.2024.1470651

TABLE 2 Results of density testing of samples produced by LPBF.

No. of regime/sample		ρ, g/cm3	ρ, g/cm3 average	δ, %	δ, % average
VZh159-250-600	1	7.89	7.89	18.6	16.7
	2	7.89		15.6	
	3	7.89		16.0	
VZh159-250-700	4	7.88	7.88	13.4	13.9
	5	7.88		13.2	
	6	7.88		15.2	
VZh159-250-800	7	7.89	7.89	16.8	16.1
	8	7.89		16.1	
	9	7.89		15.3	
VZh159-300-600	10	7.86	7.86	16.5	19.5
	11	7.86		20.5	
	12	7.86		21.4	
VZh159-300-700	13	7.88	7.88	15.3	15.6
	14	7.88		17.1	
	15	7.88		14.5	
VZh159-300-800	16	7.89	7.89	15.9	17.8
	17	7.89		19.9	
	18	7.89		17.6	
VZh159-350-600	19	7.9	7.9	19.3	19.8
	20	7.9		19.5	
	21	7.9		20.5	
VZh159-350-700	22	7.89	7.89	17.5	17.3
	23	7.89		16.4	
	24	7.89		18.0	
VZh159-350-800	25	7.91	7.91	11.5	14.1
	26	7.91		15.0	
	27	7.91		15.9	
Min		7.86	7.86	11.5	13.9
Max		7.91	7.91	21.4	19.8

material microstructure around the scan lines was investigated using a Tescan Vega scanning electron microscope.

EBSD microstructure maps of single laser scan lines on LPBF manufactured plate are presented in Figure 7. There is almost no means of accurate detection of the melt pool zones. The grain structure around single scan lines and LPBF manufactured plate are very similar, they consist of elongated curved grains having almost the same sizes and revealing no texture. The national boundary

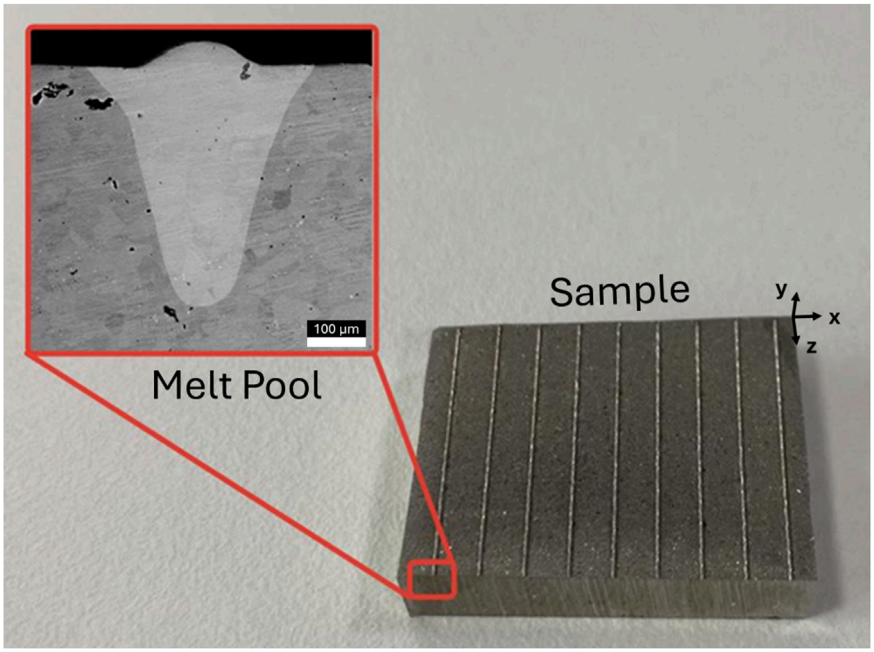

FIGURE 6
Metal plate with nine laser scan lines under different exposure regimes: view of the single scan lines on a metal plate.

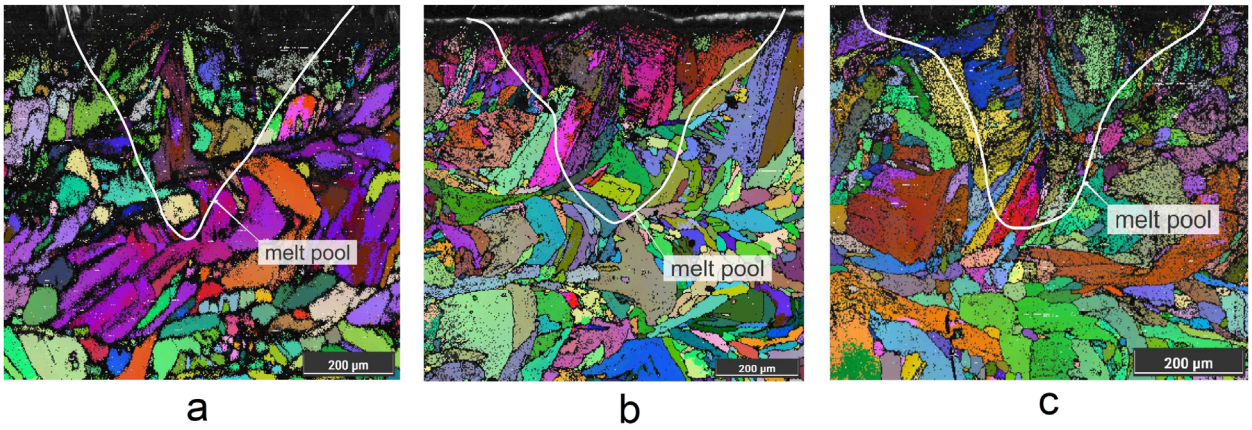

FIGURE 7
Melt pool zone of single track: **(A)** for *P*-350, *v*-600 regime, **(B)** for *P*-350, *v*-700 regime, **(C)** for *P*-350, *v*-800 regime.

of the melt pool zone is elusive in EBSD patterns although some excessive porosity may be attributed to heat affected zone in the bulk of plate.

On the other hand, EBSD analysis around single scan lines on forged plates revealed significant rearrangement of the grain structure in melt pool zones for all nine regimes. There was alignment of the grains towards the center of the heat source, associated with the focused laser beam. This grain structure rearrangement may lead to the redistribution of internal stresses in the melt pool zone and its vicinity. Beyond the fusion zone, significant changes in the grain structure were not detected, indicating decreasing influence of the laser heat source outside the melt pool boundaries (Figure 8). The greatest rearrangement of the grain structure occurs with longer laser exposure, which can result from increasing laser power and decreasing scanning speed for a single pass of the beam.

The graphical representation of the regression model for the influence of the technological parameters on the dependent variables Y_1, the depth of the melt pool (D), and Y_2, the width of the melt pool (W) is shown in Figure 9. The most significant correlation between the depth of the melt pool is found the relationship between the laser power and the scanning speed. As the laser power increases and the scanning speed decreases, the depth of the melt pool increases. The most significant impact on the width of the melt pool is due to the laser power. As the laser power and scanning speed increase, the width of the melt pool also increases.

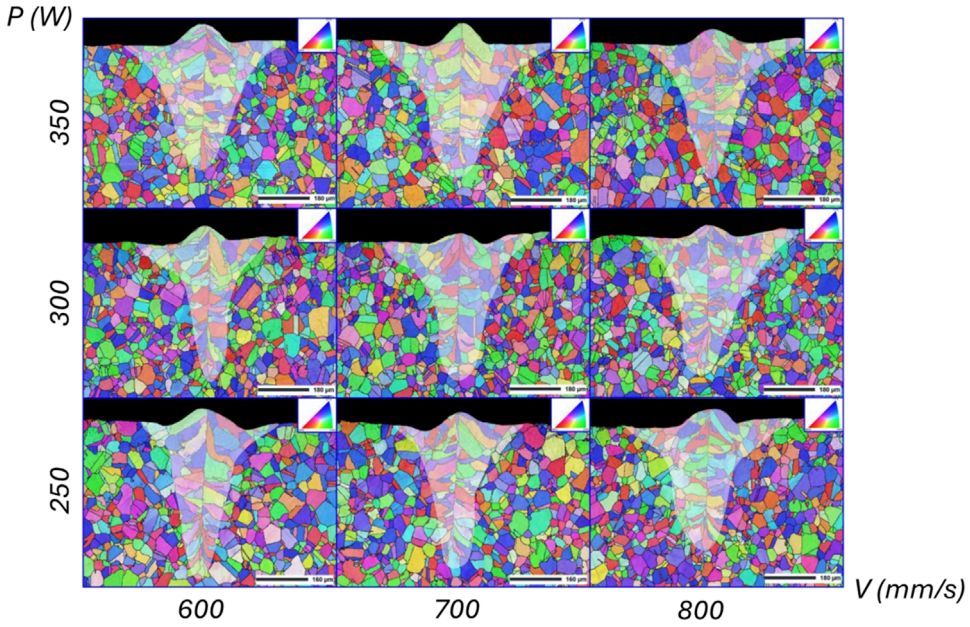

FIGURE 8
EBSD maps of the melt pool zones for the nine melting regimes – forged plate substrate.

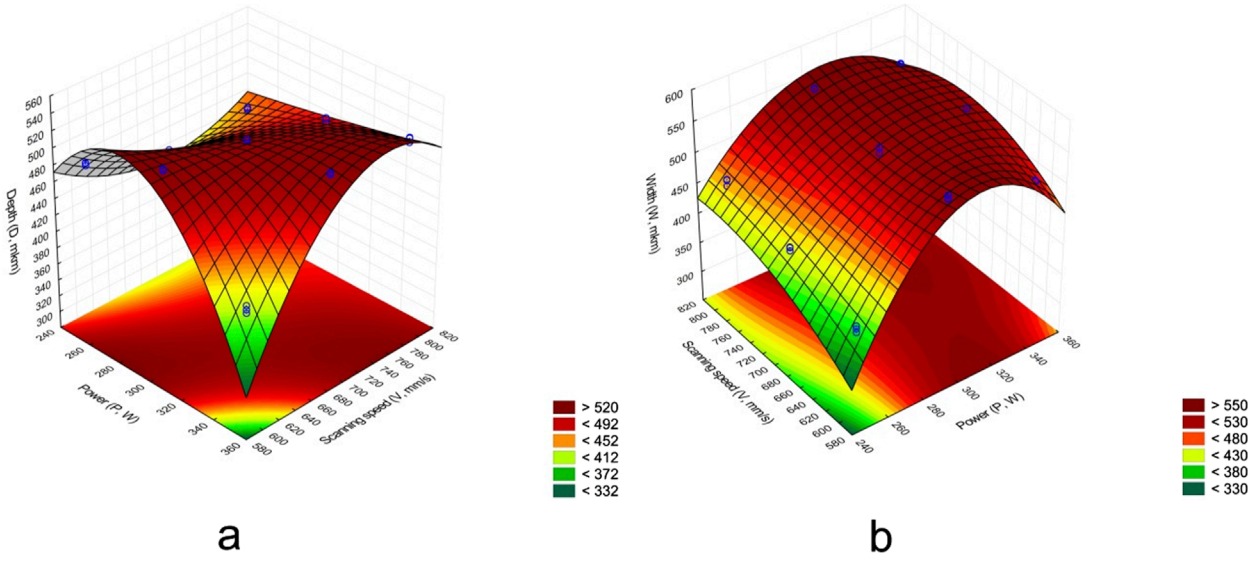

FIGURE 9
Dependence of technological parameters on: **(A)** depth of the melt pool (D), **(B)** width of the melt pool (W).

4 Discussion

The results of this study underscore the effectiveness of the full factorial analysis method in identifying optimal Laser Powder Bed Fusion (LPBF) parameters for melting VZh159 alloy with superior mechanical properties. The identified optimal parameters–laser power of 250 W, hatch distance of 0.12 mm, scanning speed of 600 mm/s, and a volumetric energy density of 69.44 J/mm^3 – were shown to produce the best mechanical properties, including ultimate tensile strength and yield stress, along with a high-quality microstructure. This optimization is critical, as LPBF parameters significantly influence the microstructural evolution and mechanical performance of the fabricated parts.

A key finding of the study was the inverse relationship between laser power and the strength characteristics of the LPBF samples. Specifically, an increase in laser power led to a decline in tensile strength, which can be attributed to excessive heat input that promotes grain growth and defect formation such as pores

and cracks. This phenomenon has been similarly observed in studies on Ni-based alloys, where excessive energy input resulted in coarser grain structures and increased porosity, negatively impacting mechanical properties (Kong et al., 2021; Qin et al., 2020; Dong et al., 2024; Salvati et al., 2020). However, EBSD analysis in this study did not reveal significant changes in grain structure, suggesting that the primary factor influencing mechanical performance is the depth of the melt pool, which facilitates optimal secondary heating and aging of the underlying layers.

In contrast, variations in scanning speed within the tested range did not significantly affect tensile strength, indicating that scanning speed is less critical than laser power in this context. This is consistent with findings from other research on Ni-based alloys, where the influence of scanning speed was found to be secondary to that of laser power and energy density in determining microstructural and mechanical outcomes (Dong et al., 2024).

The variability in yield strength observed across different LPBF regimes, particularly in samples produced under the VZh159-250-700 regime, where yield strength ranged from 983.6 MPa to 1,005.5 MPa, points to the influence of melt pool dynamics and localized thermal histories during fabrication. These variations emphasize the importance of precise control and monitoring of the LPBF process to ensure consistent mechanical properties, aligning with the need for a deeper understanding of how specific process parameters affect microstructural evolution (Mostafaei et al., 2023; Haines et al., 2022).

The measured density of the VZh159 samples showed a small deviation from the theoretical density, which indicates the presence of slight porosity but suggests satisfactory metallurgical integrity of the fabricated samples. This finding is in line with studies on Ni-based alloys that have highlighted the importance of minimizing porosity through optimized melting regimes, which are critical for achieving high density and mechanical strength (Dong et al., 2024; Juliet Martins Freitas et al., 2024). The consistent densities across different conditions reflect the stability of the melting process, reinforcing the robustness of the identified parameters.

Relative elongation also varied across different regimes, with regime No. 2 yielding the lowest average elongation (~13.9%) and regime No. 7 the highest (~19.8%). The elongation values for other regimes ranged between 14% and 17%. This indicates that while some regimes can produce highly ductile samples, others may result in relatively more brittle outcomes, influenced by the specific combination of process parameters.

The microstructural insights gained from EBSD analysis highlighted significant grain restructuring within the melt pool zones across all tested regimes, with grains aligning towards the laser source's center line. This directional solidification process is a common feature of LPBF, driven by the focused heat deposition of the laser beam, and has been shown to influence internal stress distributions and mechanical properties in similar studies on additively manufactured alloys (Zhao et al., 2022; Salvati et al., 2020). However, outside the fusion zone, the grain structure remained largely unchanged, suggesting that the thermal influence is confined to the immediate vicinity of the melt pool.

This study also points out that while single scan lines experiments provide valuable input data for computational models and a rough estimation of heat-affected zones, they are not fully representative of the complex thermal history experienced during actual LPBF manufacturing. Real manufacturing involves repeated laser interactions that result in a complex thermal environment, with multiple occurrences of melting, solidification, and recrystallization, leading to diverse microstructural transformations. Therefore, future studies should incorporate more comprehensive microstructural investigations, such as examining cellular structures and sub-grain formations, to fully elucidate the relationship between LPBF parameters, microstructure, and mechanical properties (Haines et al., 2022; Salvati et al., 2020).

In summary, this research establishes a foundational understanding of the optimal LPBF parameters for VZh159 alloy, emphasizing the delicate balance between laser power and scanning speed in achieving desirable mechanical properties. Future work should build on these findings by conducting more detailed microstructural analyses and exploring how variations in LPBF regimes impact other critical material properties. By refining the understanding of the microstructural mechanisms at play, it will be possible to further enhance the performance of LPBF-manufactured alloys, thereby broadening their application scope in advanced engineering fields.

5 Conclusion

This study presents a thorough investigation into the Laser Powder Bed Fusion (LPBF) of the VZh159 alloy, utilizing a full factorial experimental approach to establish optimal technological parameters that enhance both mechanical properties and microstructural quality. The research reveals several key insights into the LPBF process and its effects on the VZh159 alloy.

1. The study identified that the optimal LPBF parameters for VZh159 alloy include a laser power of 250 W, a scanning step of 0.12 mm, and a scanning speed of 600 mm/s, resulting in a volumetric energy density of 69.44 J/mm^3. These conditions were found to achieve the best balance between tensile strength and ductility while ensuring a high-quality microstructure in the fabricated components.
2. The analysis highlights that laser power is the most influential parameter affecting mechanical properties. Specifically, higher laser power was observed to decrease tensile strength, likely due to increased heat input leading to grain growth and defect formation. In contrast, scanning speed had a minimal impact on tensile strength within the tested range, suggesting that laser power is crucial for controlling mechanical characteristics, whereas scanning speed can be adjusted within a broader range without significantly affecting strength.
3. Significant variations in yield strength were noted within specific LPBF regimes, underscoring the need for precise control and monitoring of the LPBF process to ensure consistency in mechanical properties across different production runs. For instance, regime No. 2 exhibited yield strengths ranging from 983.6 MPa to 1,005.5 MPa, indicating the sensitivity of mechanical properties to slight variations in process parameters.
4. EBSD analysis provided valuable insights into the microstructural changes occurring within the melt pool. The

study observed significant grain restructuring within the melt pool zones, with grains aligning towards the center of the laser heat source. This restructuring was more pronounced with prolonged laser exposure, emphasizing the importance of controlling laser power and scanning speed to optimize grain structure and, consequently, mechanical properties. Notably, no significant changes were observed outside the melt pool zone, indicating minimal thermal influence beyond this area.

In summary, this study offers a comprehensive understanding of the LPBF process for VZh159 alloy, highlighting the critical role of laser power in influencing mechanical properties and microstructural quality. These findings provide a solid foundation for further refinement of LPBF parameters and suggest avenues for future research, including the exploration of additional properties such as fatigue resistance and corrosion behavior. By focusing on these areas, future studies can enhance the performance and consistency of additively manufactured nickel-based superalloys.

Data availability statement

The original contributions presented in the study are included in the article/supplementary material, further inquiries can be directed to the corresponding author.

Author contributions

RK: Conceptualization, Data curation, Investigation, Methodology, Validation, Visualization, Writing–original draft, Writing–review and editing. ES: Formal Analysis, Software, Validation, Visualization, Writing–original draft. IS: Formal Analysis, Validation, Writing–original draft, Visualization. AF: Data curation, Formal Analysis, Software, Visualization, Writing–original draft. AS: Conceptualization, Data curation, Funding acquisition, Project administration, Resources, Supervision, Writing–original draft, Writing–review and editing, Investigation, Methodology, Software, Validation. AK: Conceptualization, Data curation, Funding acquisition, Investigation, Project administration, Resources, Supervision, Writing–original draft, Writing–review and editing, Formal Analysis, Methodology, Software, Validation.

Funding

The author(s) declare that financial support was received for the research, authorship, and/or publication of this article. This study was carried out under the Agreement for the provision of grant funding from the federal budget for large scientific projects in priority areas of scientific and technological development of the Russian Ministry of Science and Higher Education no. 075-15-2024-552.

Conflict of interest

The authors declare that the research was conducted in the absence of any commercial or financial relationships that could be construed as a potential conflict of interest.

Publisher's note

All claims expressed in this article are solely those of the authors and do not necessarily represent those of their affiliated organizations, or those of the publisher, the editors and the reviewers. Any product that may be evaluated in this article, or claim that may be made by its manufacturer, is not guaranteed or endorsed by the publisher.

References

Adegoke, O., Andersson, J., Brodin, H., and Pederson, R. (2020). Review of laser powder bed fusion of gamma-prime-strengthened nickel-based superalloys. *Metals* 10, 996. doi:10.3390/met10080996

Aota, L. S., Bajaj, P., Sandim, H. R. Z., and Jägle, E. A. (2020). Laser Powder-Bed Fusion as an Alloy Development tool: parameter selection for *In-Situ* alloying using elemental powders. *Materials* 13 (18), 3922. doi:10.3390/ma13183922

Badoniya, P., Srivastava, M., Jain, P. K., and Rathee, S. (2024). A state-of-the-art review on metal additive manufacturing: milestones, trends, challenges and perspectives. *J. Braz. Soc. Mech. Sci. Eng.* 46 (6), 339. doi:10.1007/s40430-024-04917-8

Bernard, A., Kruth, J.-P., Cao, J., Lanza, G., Bruschi, S., Merklein, M., et al. (2023). Vision on metal additive manufacturing: developments, challenges and future trends. *CIRP J. Manuf. Sci. Technol.* 47, 18–58. doi:10.1016/j.cirpj.2023.08.005

Bologna, O., Cecchel, S., Cornacchia, G., Avanzini, A., Sepe, R., Berto, F., et al. (2024). Investigating post-processing impact on fatigue performance of LPBF Ti6Al4V with heat treatment, high pressure heat treatment, and dry electropolishing strategies. *Int. J. Fatigue* 185, 108365. doi:10.1016/j.ijfatigue.2024.108365

Cao, L., Li, J., Hu, J., Liu, H., Wu, Y., and Zhou, Q. (2021). Optimization of surface roughness and dimensional accuracy in LPBF additive manufacturing. *Opt. Laser Technol.* 142, 107246. doi:10.1016/j.optlastec.2021.107246

Dimopoulos, A., Salimi, M., Gan, T.-H., and Chatzakos, P. (2023). Support structures optimisation for high-quality metal additive manufacturing with laser powder bed fusion: a numerical simulation study. *Materials* 16 (22), 7164. doi:10.3390/ma16227164

Dinița, A., Neacșa, A., Portoacă, A. I., Tănase, M., Ilinca, C. N., and Ramadan, I. N. (2023). Additive manufacturing post-processing treatments, a review with emphasis on mechanical characteristics. *Materials* 16 (13), 4610. doi:10.3390/ma16134610

Dong, Z., Han, C., Zhao, Y., Huang, J., Ling, C., Hu, G., et al. (2024). Role of heterogenous microstructure and deformation behavior in achieving superior strength-ductility synergy in zinc fabricated via laser powder bed fusion," *Int. J. Extrem. Manuf.*, 6, 045003. doi:10.1088/2631-7990/ad3929

Evangelou, A., Stylianou, R., Loizou, A., Kim, D., Liang, A., Reed, P., et al. (2023). Effects of process parameters and scan strategy on the microstructure and density of stainless steel 316 L produced via laser powder bed fusion. *J. Alloys Metallurgical Syst.* 3, 100027. doi:10.1016/j.jalmes.2023.100027

Ge, J., Pillay, S., and Ning, H. (2023). Post-process treatments for additive-manufactured metallic structures: a comprehensive review. *J. Mater. Eng. Perform.*, 32 (16), 7073–7122. doi:10.1007/s11665-023-08051-9

Gibbons, D. W., Serfontein, J.-P. L., and Van Der Merwe, A. F. (2021). Mapping the path to certification of metal laser powder bed fusion for aerospace applications. *Rapid Prototyp. J.* 27 (2), 355–361. doi:10.1108/rpj-07-2020-0154

Gokcekaya, O., Ishimoto, T., Todo, T., Wang, P., and Nakano, T. (2021). Influence of powder characteristics on densification via crystallographic texture formation: pure tungsten prepared by laser powder bed fusion. *Addit. Manuf. Lett.* 1, 100016. doi:10.1016/j.addlet.2021.100016

Haines, M. P., Rielli, V. V., Primig, S., and Haghdadi, N. (2022). Powder bed fusion additive manufacturing of Ni-based superalloys: a review of the main

microstructural constituents and characterization techniques. *J. Mater Sci.* 57, 14135–14187. doi:10.1007/s10853-022-07501-4

Hasanabadi, M., Keshavarzkermai, A., Asgari, H., Azizi, N., Gerlich, A., and Toyserkani, E. (2023). *In-situ* microstructure control by laser post-exposure treatment during laser powder-bed fusion. *Addit. Manuf. Lett.* 4, 100110. doi:10.1016/j.addlet.2022.100110

Huang, R.-Y., Lu, J.-Q., Cheng, C.-W., Tsai, M.-C., and Lee, A.-C. (2024). Multi-data-driven model-based control to improve the accuracy of overhang structures in laser powder bed fusion. *Opt. and Laser Technology/Optics Laser Technol.* 171, 110398. doi:10.1016/j.optlastec.2023.110398

Juliet Martins Freitas, B., Yuuki Koga, G., Arneitz, S., Bolfarini, C., and de Traglia Amancio-Filho, S. (2024). Optimizing LPBF-parameters by Box-Behnken design for printing crack-free and dense high-boron alloyed stainless steel parts. *Addit. Manuf. Lett.* 9, 100206. doi:10.1016/j.addlet.2024.100206

Kablov, E. N., Evgenov, A. G., Mazalov, I. S., Shurtakov, S. V., Zaitsev, D. V., and Prager, S. M. Evolution of the structure and properties of high-chromium heat-resistant VZh159 alloy prepared by selective laser melting: Part II: *Appl. Res.* 2020, 11 (1), 17–24. doi:10.1134/s2075113320010165

Khanna, N., Zadafiya, K., Patel, T., Kaynak, Y., Rashid, R. A. R., and Vafadar, A. (2021). Review on machining of additively manufactured nickel and titanium alloys. *J. Mater. Res. Technology/Journal Mater. Res. Technol.* 15, 3192–3221. doi:10.1016/j.jmrt.2021.09.088

Khorasani, A. M., Gibson, I., Ghasemi, A., and Ghaderi, A. (2020). Modelling of laser powder bed fusion process and analysing the effective parameters on surface characteristics of Ti-6Al-4V. *Int. J. Mech. Sci.* 168, 105299. doi:10.1016/j.ijmecsci.2019.105299

Kong, Dc., Dong, Cf., Ni, Xq, Zhang, L., Li, R. x., He, X., et al. (2021). Microstructure and mechanical properties of nickel-based superalloy fabricated by laser powder-bed fusion using recycled powders. *Int. J. Min. Metall. Mater* 28, 266–278. doi:10.1007/s12613-020-2147-4

Kyarimov, R. R., Smelov, V., and Alekseev, V. (2023). Study of the structure and mechanical properties of samples produced by the method of selective laser melting from metallic powder of heat-resistant alloy VZh159 (KhN58MBYu). *Sci. Tech. J.* 25, 36–46. doi:10.37313/1990-5378-2023-25-4-36-46

Lankin, A. M., and Shaikhutdinov, D. V. (2015). *Experimental planning in scientific research: guidelines for laboratory work, Novocherkassk: srspu*, 42.

Livera, E. R., Christofidou, K., Miller, J. R., Chechik, L., Ryan, D., Shrive, J., et al. (2024). Microstructural control of LPBF Inconel 718 through post processing of intentionally placed AM discontinuity distributions. *Materialia* 36, 102163. doi:10.1016/j.mtla.2024.102163

LPBF (2024). Free supports strategy for LPBF 3D printing process. Available at: https://www.thesteelprinters.com/news/free-supports-strategy-for-lpbf-3d-printing.

Materials for additive technological processes (2024). Control and test methods of metal raw materials and products [Electronic resource]. Available at: https://docs.cntd.ru/document/1200157656.

Mostafaei, A., Ghiaasiaan, R., Ho, I. T., Strayer, S., Chang, K. C., Shamsaei, N., et al. (2023). Additive manufacturing of nickel-based superalloys: a state-of-the-art review on process-structure-defect-property relationship. *Prog. Mater. Sci.* 136, 101108. doi:10.1016/j.pmatsci.2023.101108

Novik, F. S., and Arsov, Y. B. (1980). *Optimization of metal technology processes using experimental design methods*. Germany: Mechanical Engineering Publishing House.

Pant, M., Moona, G., Nagdeve, L., and Kumar, H. (2023). Dimensional accuracy and stability analysis of laser powder bed fusion (LPBF) samples: implications of process variables. *IJIDEM*, 18 (3), 1121–1129. doi:10.1007/s12008-023-01680-3

Pant, P., Salvemini, F., Proper, S., Luzin, V., Simonsson, K., Sjöström, S., et al. (2022). A study of the influence of novel scan strategies on residual stress and microstructure of L-shaped LPBF IN718 samples. *Mater. and Des.* 214, 110386. doi:10.1016/j.matdes.2022.110386

Paraschiv, A., Matache, G., Condruz, M. R., Frigioescu, T. F., and Pambaguian, L. (2022). Laser powder bed fusion process parameters' optimization for fabrication of dense in 625. *Materials* 15 (16), 5777. doi:10.3390/ma15165777

Pelevin, I. A., Terekhin, E. A., Ozherelkov, D.Yu., Tereshina, I. S., Karpenkov, D.Yu., Bochkanov, F.Yu., et al. (2023). New scanning strategy approach for Laser Powder bed fusion of ND-FE-B hard magnetic material. *Metals* 13 (6), 1084. doi:10.3390/met13061084

Prashar, G., Vasudev, H., and Bhuddhi, D. (2022). Additive manufacturing: expanding 3D printing horizon in industry 4.0. *IJIDEM* 17 (5), 2221–2235. doi:10.1007/s12008-022-00956-4

Qin, Y., Lou, S., Shi, P., Qi, Q., Zeng, W., Scott, P. J., et al. (2023). Optimisation of process parameters for improving surface quality in laser powder bed fusion. *Int. J. Adv. Manuf. Technol.* 130 (5–6), 2833–2845. doi:10.1007/s00170-023-12826-8

Qin, Y., Wen, P., Xia, D., Guo, H., Voshage, M., Jauer, L., et al. (2020). Effect of grain structure on the mechanical properties and *in vitro* corrosion behavior of additively manufactured pure Zn," *Addit. Manuf.*, 33, 101134. doi:10.1016/j.addma.2020.101134

Rafael De Sa Barros (2019). Laser powder bed fusion of IN718: optimization of process parameters and residual stress analysis before and after heat treatment. Available at: https://core.ac.uk/download/pdf/302874251.pdf.

Ruan, G., Liu, C., Qu, H., Guo, C., Li, G., Li, X., et al. (2022). A comparative study on laser powder bed fusion of IN718 powders produced by gas atomization and plasma rotating electrode process. *Mater. Sci. Eng. A* 850, 143589. doi:10.1016/j.msea.2022.143589

Salvati, E., Lunt, A. J. G., Heason, C. P., Baxter, G. J., and Korsunsky, A. M. (2020). An analysis of fatigue failure mechanisms in an additively manufactured and shot peened IN 718 nickel superalloy. *Mater. Des.* 191, 108605. doi:10.1016/j.matdes.2020.108605

Senvol Database (2024). Senvol database in Granta selector. Available at: https://innovationspace.ansys.com/knowledge/forums/topic/what-is-senvol-database-in-granta-selector/.

Shrivastava, A., S, A. K., Rao, S., Bk, N., Barad, S., and Tn, S. (2021). Remanufacturing of nickel-based aero-engine components using metal additive manufacturing technology. *Mater. Today Proc.*, 45, 4893–4897. doi:10.1016/j.matpr.2021.01.355

Taylor, H. C., Garibay, E. A., and Wicker, R. B. (2021). Toward a common laser powder bed fusion qualification test artifact. *Addit. Manuf.* 39, 101803. doi:10.1016/j.addma.2020.101803

U.S. department of transportation (2024). Powder bed fusion additive manufacturing process for aircraft engine parts. Available at: https://www.faa.gov/documentLibrary/media/Advisory_Circular/AC_33.15-3.pdf.

Yong, C. K., Gibbons, G. J., Wong, C. C., and West, G. (2020). A Critical review of the material characteristics of additive manufactured IN718 for High-Temperature Application. *Metals*, 10 (12), 1576. doi:10.3390/met10121576

Zhao, Y., Guo, Q., Du, Z., Chen, S., Tan, J., Yang, Z., et al. (2022). Critical role of subgrain orientation on the stability of mechanical properties of selective laser melting manufactured alloys," *Mater. Sci. Eng. A*. 832, 142505. doi:10.1016/j.msea.2021.142505